Coherent anti-Stokes Raman scattering microscopy of single nanodiamonds

Iestyn Pope,[1] Lukas Payne,[1] George Zoriniants,[1] Evan Thomas,[2] Oliver Williams,[2] Peter Watson,[1] Wolfgang Langbein,[2] and Paola Borri[1,*]

[1] *Cardiff University School of Biosciences, Museum Avenue, Cardiff CF10 3AX, United Kingdom*

[2] *Cardiff University School of Physics and Astronomy, The Parade, Cardiff CF24 3AA, United Kingdom*

(Dated: August 14, 2014)

Abstract

Nanoparticles have attracted enormous attention for biomedical applications as optical labels, drug delivery vehicles, and contrast agents *in vivo*. In the quest for superior photostability and bio-compatibility, nanodiamonds (NDs) are considered one of the best choices due to their unique structural, chemical, mechanical, and optical properties. So far, mainly fluorescent NDs have been utilized for cell imaging. However, their use is limited by the efficiency and costs in reliably producing fluorescent defect centers with stable optical properties. Here, we show that single non-fluorescing NDs exhibit strong coherent anti-Stokes Raman scattering (CARS) at the sp^3 vibrational resonance of diamond. Using correlative light and electron microscopy, the relationship between CARS signal strength and ND size is quantified. The calibrated CARS signal in turn enables the analysis of the number and size of NDs internalized in living cells *in situ*, which opens the exciting prospect of following complex cellular trafficking pathways quantitatively.

Nanodiamonds can be fabricated with a variety of particle sizes in the 5-500 nm range via relatively inexpensive methods, including the detonation of carbon containing explosives or milling of synthetic micron-sized monocrystalline diamond particles [1, 2]. They have shown high biocompatibility in many cell lines and animal models with minimal or no cytotoxicity [3], and are efficiently internalized in cells even with sizes in the 100 nm range without disruption of cellular functions such as division and differentiation [4–6]. They also take advantage of the rich chemistry of organic functional groups such as carboxyl at their surface to enable covalent binding of biomolecules for target-specific labelling [7].

For applications in optical microscopy, mainly fluorescent NDs have been utilised where the fluorescence originates from the presence of nitrogen vacancy (NV) centers - a nitrogen atom next to a lattice vacancy [2, 4, 8, 9]. Their use is however limited by the efficiency and costs in producing NV centers in NDs, which require sufficient nitrogen atoms in the diamond lattice and an efficient generation of vacancies (e.g. via high energy electron irradiation) to achieve a nitrogen-vacancy pair in atomic proximity. Moreover, NV centers might irreversibly change their fluorescence properties upon photoexcitation (for example by conversion of negative NV^- vacancies into neutral NV^0 [10, 11]), and when close to the ND surface they might become unstable. To date, only a few studies have been reported on the visualization of non-fluorescing NDs in cells using differential interference contrast (DIC) microscopy [12] or Raman scattering at the sp^3 diamond vibrational resonance (1332/cm) [13]. However, DIC is unspecific and fairly large ND ensembles are required to achieve sufficient optical phase contrast to distinguish them from the cellular environment. Conversely, confocal Raman micro-spectroscopy is chemically specific but notoriously slow and hardly compatible with imaging living cells.

Coherent anti-Stokes Raman scattering microscopy has emerged in the last decade as a novel chemically-specific technique which overcomes the speed-limit of spontaneous Raman microscopy owing to the constructive interference of Raman scattered light by identical vibrational modes coherently driven in the CARS excitation process (for a recent review see [14]). Briefly, CARS is a third-order nonlinear process (four-wave mixing) in which two laser fields of frequencies ν_P (Pump) and ν_S (Stokes) coherently drive a molecular vibration in resonance at the frequency difference $\nu_{vib} = \nu_P - \nu_S$. The CARS field at the frequency $2\nu_P - \nu_S = \nu_P + \nu_{vib}$ is the anti-Stokes scattering of the Pump field by the coherently driven vibration. Being a nonlinear process, CARS exhibits high spatial resolution beyond the

one-photon diffraction limit and offers intrinsic optical sectioning. Furthermore, CARS is free from (one-photon) autofluorescence backgrounds since its frequency is higher than the excitation field frequencies. CARS emission is also highly photostable since no electronic excitation is usually created. Owing to the sharp Raman peak of diamond at 1332/cm and the large number of identical sp^3 bonds in a ND (a 10 nm diamond particle has about 10^5 C-C pairs) one would expect a significant CARS signal enhancement to occur and in turn rapid chemically-specific imaging of non fluorescing NDs in living cells to become possible. However, to the best of our knowledge no CARS studies on NDs have been reported to date.

In this work, we report a quantitative study of the CARS signal strength from single non-fluorescing NDs imaged with CARS alongside DIC, dark-field, optical extinction microscopy, and electron microscopy. Correlative measurements were performed on the same single NDs to quantify the relationship between ND size and its non-fluorescing optical properties and in particular to determine the CARS detection sensitivity limit. Proof-of-principle quantitative imaging of NDs in living cells is also shown.

CONFOCAL RAMAN MICRO-SPECTROSCOPY

Firstly, we verified that the investigated NDs exhibit the sp^3 diamond vibrational resonance by confocal Raman micro-spectroscopy as shown in Fig. 1. It is well documented that Raman spectroscopy provides insight on the purity of NDs in terms of the ratio between the sp^3 bulk diamond group and the sp^2 surface carbon. In particular, the spectra of NDs with a high sp^2 carbon content are dominated by the D and G bands of graphitic carbon at around 1400/cm and 1600/cm respectively while the sp^3 diamond resonance at 1332/cm is weak and broadened [2]. Surface functional groups of air-oxidized NDs also contribute to broad spectral features at around 1600/cm. We clearly observe a sharp (resolution limited) sp^3 diamond peak at 1332/cm in the investigated NDs, similar to that measured in a bulk diamond sample. Phonon confinement effects, giving rise to a shift and broadening of the peak, are significant only for NDs smaller than about 10 nm [15]. Bands from ND surface groups are present in the 1400-1600/cm range but are of relatively minor importance indicating a good core crystal-volume-to-surface ratio. The structural morphology of a typical monocrystalline single ND in the investigated sample is shown with transmission electron microscopy in Fig. 1a.

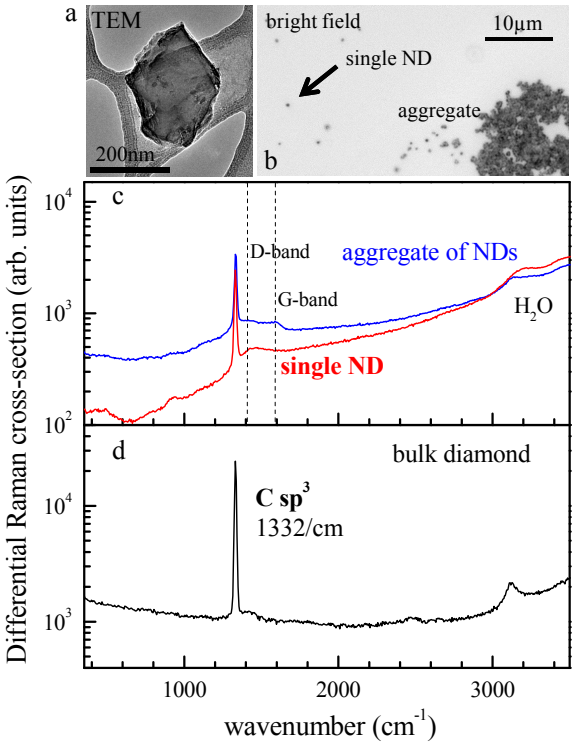

FIG. 1. **Raman micro-spectroscopy of nanodiamonds.** **a**, Transmission electron microscopy (TEM) of a single ND onto a hollow EM carbon film; **b**, bright field optical microscopy of NDs in water, drop-cast onto a glass coverslip. **c**, Raman micro-spectroscopy on the ND aggregate and single ND indicated on the top panel. **d**, Raman micro-spectroscopy of a bulk diamond sample. The sharp (resolution limited) sp^3 bulk diamond peak at 1332/cm is well visible also in the NDs indicating the presence of a significant diamond crystal core.

CORRELATIVE OPTICAL EXTINCTION CROSS-SECTION AND SEM

We then measured the extinction cross-section of single NDs using a quantitative wide-field microscopy technique recently demonstrated by us [16] (see also supplementary information, S2). NDs were covalently bound onto a gridded coverslip which enabled subsequent correlative scanning electron microscopy (SEM) on the same NDs. An example of this correlative imaging is shown in Fig. 2. On the top panel (Fig. 2a), SEM on a region containing 3 structures is shown. Two of the structures appear as small aggregates, while a zoom onto the smaller structure reveals a single ND. A full color (RGB) dark-field image acquired with white-light illumination and a color camera over the same region is shown in the middle panel (Fig. 2b). NDs scatter due to their refractive index of 2.4 which is nearly independent

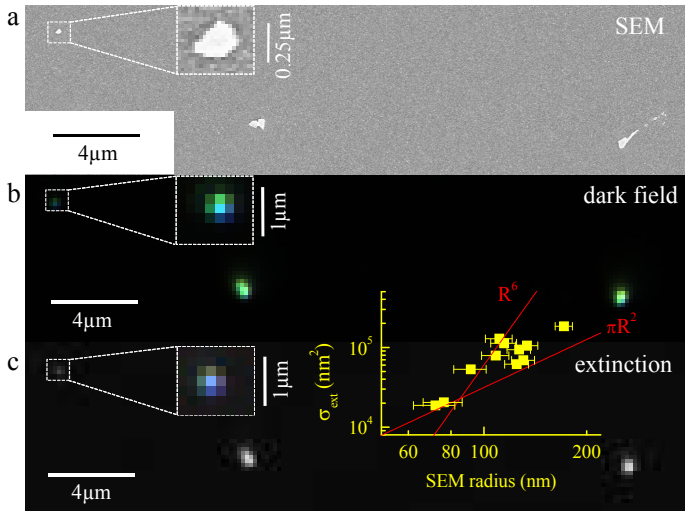

FIG. 2. **Optical extinction of single NDs versus size.** **a**, SEM image of a region containing few ND structures, together with a zoom over an isolated ND. **b**, Full color (FC) dark-field image of the same region as in the top panel. **c**, FC extinction image from -0.02 to 0.042 over the brightness range of each color, for the same region as in the middle and top panel. The zoomed extinction image is from -0.02 to 0.017. The lateral color displacement in the dark-field and extinction images is due to lateral chromatic aberrations in the objective. Inset: extinction cross-section measured from the extinction image (see text) versus ND radius calculated from the area measured in SEM being equated to that of a disk. The error bar accounts for the uncertainty in the thickness of the deposited gold layer needed to perform SEM on NDs.

of wavelength (as opposed to gold nanoparticles [16] which selectively scatter in the green due to their plasmonic properties). The bottom panel (Fig. 2c) shows the extinction image defined as $\Delta = (I_\mathrm{d} - I_\mathrm{f})/I_\mathrm{d}$ with I_f being the background-subtracted transmitted intensity of the bright-field image with NDs in focus and I_d the corresponding image out-of-focus. The extinction cross section measured as $\sigma_\mathrm{ext} = \int_{A_\mathrm{i}} \Delta dA$ (plus a local background correction as described in [16]) is shown in the inset as a function of ND radius R deduced from the measured SEM area as πR^2 (note that since NDs are non absorbing their extinction cross-section is a direct measure of their scattering cross-section). σ_ext is scaling with a R^6 dependence for small ND sizes, as one would expect for the scattering cross-section of small particles in the Rayleigh limit. This changes toward a dependence scaling like the physical ND area when the ND sizes become comparable to the light wavelength.

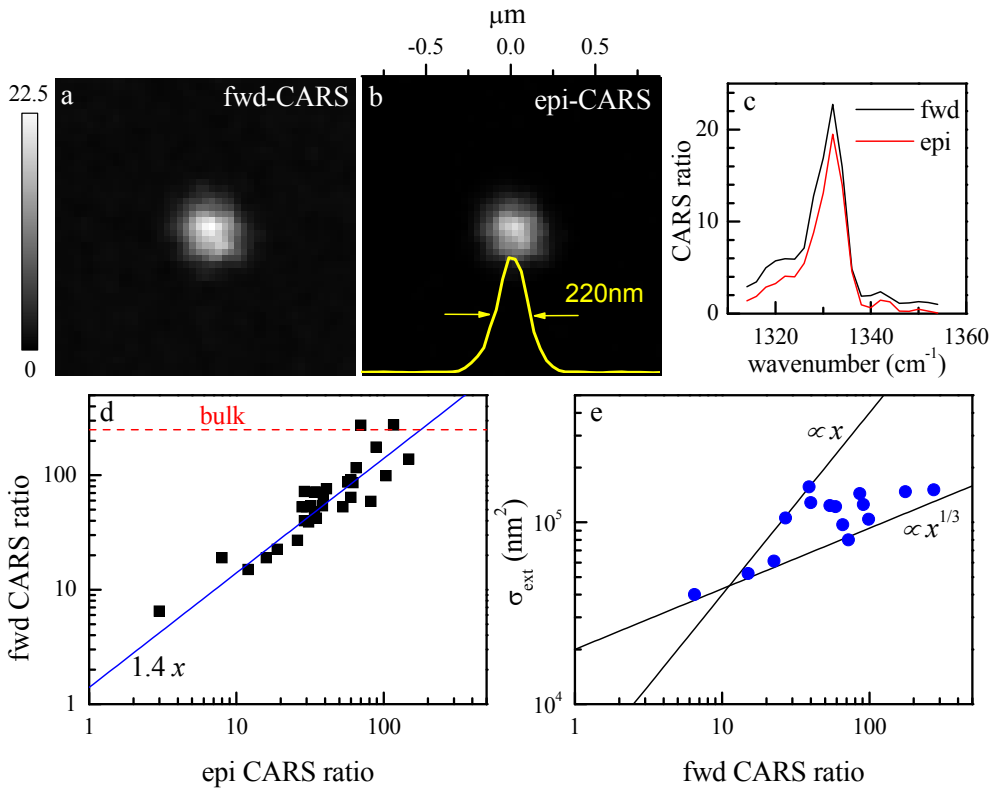

FIG. 3. **CARS micro-spectroscopy of single NDs.** **a**, **b**, Two-dimensional xy CARS images of a single ND at the optimum z focal plane, collected in forward and epi direction respectively. The grey scale shows the corresponding CARS intensity ratio calculated by dividing the CARS intensity with the fwd-collected intensity in the water medium outside the ND. The yellow line in **b** is an equatorial line-cut showing a ND size limited by the microscope resolution. Pump (Stokes) power on the sample was 22 mW (15 mW). 38 nm pixel size. 0.1 ms pixel dwell time. **c**, Spectrum of fwd and epi CARS ratio at the ND spatial location. **d**, Correlation between fwd-CARS and epi-CARS intensity ratios measured simultaneously on a series of single NDs. The fwd-CARS ratio measured on a bulk diamond sample is shown as red-dotted line for comparison. **e**, Correlation between extinction cross-section and fwd-CARS ratio on the same NDs as in **d**.

CARS MICRO-SPECTROSCOPY OF SINGLE NANODIAMONDS

CARS micro-spectroscopy on single NDs in water covalently bound onto a coverslip was performed using a home built set-up which enables hyperspectral imaging with 10/cm resolution via spectral focussing from a single broadband 5 fs Ti:Sa laser source and a CARS spatial resolution (full-width at half-maximum-FWHM of the intensity point-spread func-

tion) of about 0.2 μm and 0.65μm in the lateral (xy) and axial (z) direction, respectively (for more details see Ref. [17]). CARS was simultaneously collected in both forward (fwd) and epi-direction. Full 3D xyz images were acquired to locate the NDs in the optimum focal plane, and a series of xy images at variable frequencies in the 1300-1400/cm range was then recorded to resolve the diamond vibrational resonance. An example of a xy image at the optimum focal plane on a single resolution-limited ND at the sp^3 vibrational resonance peak of 1332/cm is shown in Fig. 3 together with the corresponding CARS spectrum at the ND spatial location. Fwd-CARS spectra from the region surrounding the NDs were used for normalization i.e. the measured CARS intensity at the ND was divided by the corresponding non-resonant CARS intensity in the surrounding water under the same excitation and detection conditions in order to correct for the varying temporal overlap of pump and Stokes and to derive a CARS intensity ratio independent of excitation/detection parameters. Note that the epi-collected CARS is free from non-resonant background as expected from the directionality of CARS in a bulk medium, therefore epi-CARS ratios were also calculated relative to the non-resonant CARS intensity simultaneously measured in the fwd-direction. The CARS spectral lineshape in Fig. 3c is dominated by the peak profile of the resonant contribution in both forward and epi-direction denoting a substantial CARS signal strength (intensity ratio $\sim$ 20) from a single ND. A fwd-CARS intensity ratio of 250 was measured on a bulk diamond sample, as shown for comparison in Fig. 3. By measuring on a series of single NDs with variable sizes we found a good correlation between fwd-CARS and epi-CARS ratios with a proportionality factor of $\sim$ 1.4 (see Fig. 3d) which is explained by the slightly worse detection efficiency in the de-scanned epi-direction compared to non de-scanned forward transmission. σ_{ext} measured on the same NDs also correlates with the CARS intensity ratio with a dependence which is consistent with Fig. 2 when assuming that the CARS intensity ratio scales like the square of the ND volume, as would be expected for NDs in the size range investigated here (see also Fig.4). A proportionality between σ_{ext} and the CARS ratio thus equates to $\sigma_{\text{ext}} \propto R^6$ which is consistent with Fig. 2 for not too large NDs ($R \leq 120\,\text{nm}$).

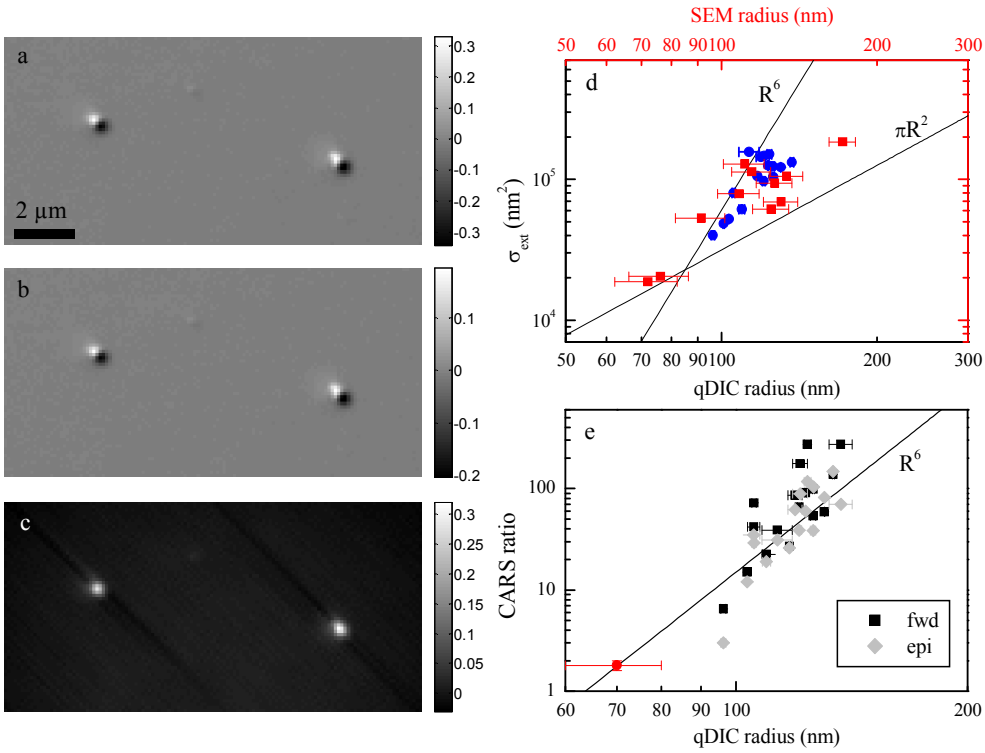

FIG. 4. **Quantitative DIC of single NDs.** **a**, DIC contrast image I_c of two NDs (the left one is the same shown in the CARS image in Fig 3a,b) and corresponding differential phase δ (**b**) and integrated optical phase φ (**c**). **d**, Extinction cross-section σ_{ext} versus ND radius as measured from DIC (blue symbols, lower x-axis), compared with the results from SEM (red symbols, upper x-axis). **e**, CARS ratio versus ND radius from DIC. The red data point shows the fwd-CARS ratio measured on smaller single NDs from a different supplier where the nominal average ND size and size distribution from the manufacturer are used as ND radius and error bar.

CORRELATIVE QUANTITATIVE DIC AND CARS

To gain further quantitative insights on the relationship between CARS signal strength and the ND size, we performed DIC on the same ND series of Fig. 3. DIC microscopy measures the difference of the optical phase between two points in the sample plane, spatially separated by an amount (the shear) typically comparable with the optical resolution. Based on this principle, we have recently developed a quantitative DIC (qDIC) image acquisition and analysis procedure to measure the spatial distribution of the optical phase [18] which for NDs of known refractive index can in turn be used to calculate their volume. In Fig. 4a we show the qDIC contrast image I_c of two NDs (the left one is the same shown in the

CARS image in Fig 3a,b) and the corresponding differential phase δ and integrated optical phase φ images. The contrast image is defined as $I_c = (I_+ - I_-)/(I_+ + I_-)$ where $I_\pm$ are the transmitted intensities for opposite angles of the polarizer in a DIC with a de Sénarmont compensator (see supplementary information, S4). The differential phase is $\delta = \varphi_+ - \varphi_-$ with $\varphi_\pm = \varphi(\mathbf{r} \pm \mathbf{s}/2)$ being the optical phase accumulated in the sample for the beam passing through the point $\mathbf{r} \pm \mathbf{s}/2$ where $\mathbf{s}$ is the shear vector and $\mathbf{r}$ is the DIC image coordinate in the sample plane. We calculate δ using the exact analytical solution of the relationship between I_c and δ (see supplementary information, S4). The spatial distribution of the optical phase at the sample $\varphi(\mathbf{r})$ is then calculated from δ by performing a Wiener deconvolution procedure [18]. The ND volume is finally calculated from the integral (A) of $\varphi(\mathbf{r})$ over the ND area. By taking into account that the optical phase introduced by a ND is $\varphi(\mathbf{r}) = 2\pi\Delta n t(\mathbf{r})/\lambda_0$ with the wavelength in vacuum λ_0, the refractive index change between the ND and its surrounding medium Δn, and the thickness profile of the ND $t(\mathbf{r})$, A is simply proportional to the ND volume V via $A = 2\pi\Delta n V/\lambda_0$. An effective ND radius R can then be deduced by assuming $V = (4/3)\pi R^3$ and in Fig. 4d,e we show the corresponding dependence of σ_{ext} and of the CARS ratio on this radius. The dependence of σ_{ext} is in good agreement with that found with SEM shown in Fig. 2, confirming the validity of our qDIC method. The error bars in the qDIC radius take into account that NDs might be sufficiently asymmetric in plane to exhibit different DIC contrast for different orientations relative to the polarization of the light field. They were obtained by measuring the qDIC radius for two orthogonal sample orientations. Fig. 4e finally shows the dependence of the CARS ratio on the ND radius. We find that an R^6 dependence is well followed for ND radii below about 120 nm while a deviation is observed for larger radii especially in the forward direction which might be attributed to the increased directionality of the fwd-CARS emission in the transition from small to large scatterers compared to the wavelength of light [14].

From the calibrated dependence of the CARS intensity ratio on ND size shown in Fig. 4e we can now estimate a lower size limit $R_{\min}$ for CARS imaging of single NDs. If $R_{\min}$ is sufficiently small the fwd-CARS will be dominated by the non-resonant CARS background and we can express the CARS intensity ratio as $\overline{I}_{\text{CARS}} = |1 + \chi_{\text{R}}/\chi_{\text{NR}}|^2 \simeq 1 + |\chi_{\text{R}}/\chi_{\text{NR}}|$ with χ_{R} (χ_{NR}) vibrationally resonant (non-resonant) third-order susceptibility. At the signal (S) to noise (N) limit we can then express $|\chi_{\text{R}}/\chi_{\text{NR}}| \simeq N/S$. From the calibration in Fig. 4e we find $\overline{I}_{\text{CARS}} \simeq 50$ for a radius $R = 120$ nm from which we deduce $|\chi_{\text{R}}/\chi_{\text{NR}}| \simeq 7$ since in this

regime $\overline{I}_{\mathrm{CARS}} \simeq |\chi_{\mathrm{R}}/\chi_{\mathrm{NR}}|^2$. Hence based on the R^3 scaling of $|\chi_{\mathrm{R}}/\chi_{\mathrm{NR}}|$ we can rewrite for R_{min} that $N/S = 7(R_{\mathrm{min}}/120)^3$. In the photon shot noise limit $N/S = 1/\sqrt{n}$ where $n = \nu\tau$ is the photon number, ν is the photon rate and τ is the acquisition time. Under the excitation and detection conditions of the CARS experiments in Fig. 3 we have $\nu = 1.5 \times 10^6$ Hz, $\tau = 0.1$ ms per pixel, hence $n = 150$. In these conditions we find $R_{\mathrm{min}} = 27$ nm. R_{min} can be further reduced by increasing the excitation intensity and/or the acquisition time (for example by averaging over several pixels in the image) since it scales as $[(I_{\mathrm{p}})^2 I_{\mathrm{s}}\tau]^{-1/6}$ where I_{p} and I_{s} are the intensities of Pump and Stokes beams respectively. This estimate thus indicate that single small NDs of sizes well compatible with intracellular trafficking in living cells can be imaged by CARS. Notably, although small nanoparticles of < 10 nm are useful as biolabels offering sizes comparable to fluorescent proteins or dyes, there are important complementary applications for larger particles. For instance, it is currently thought that the diameter of nanoparticle therapeutics for cancer should be in the range of 10-150 nm [19]. These particles should have access to and within disseminated tumors when dosed into the circulatory system. By being > 10 nm they will be restricted from exiting normal vasculature; however they will still be able to access for example the liver. It has been shown that entities in the order of hundreds of nanometers in size can leak out of the blood vessels and accumulate within tumors [19]. Moreover, the photostable CARS signal can be mapped into a *quantitative* measure of the ND size for single particles, or of the ND number for particle aggregates of known size. This direct *in situ* determination of the ND size inside living cells is not possible with fluorescent techniques which rely on nominal particle sizes, and might be affected by significant size distributions as well as aggregation. For example, in Ref. [9] nominally 45 nm diameter fluorescent NDs showed a degree of particle aggregation with 140 nm average size measured by dynamic light scattering in the suspension before incubation in cells. Furthermore, fluorescence readouts are subject to photo-bleaching or blinking. Owing to the high biocompatibility of NDs, CARS imaging opens the exciting prospect of enabling a more quantitative analysis of complex trafficking pathways in living cells for applications in drug delivery and therapeutics. We should, however, comment that when looking at commercially available NDs (Microdiamant AG) of radii below about 70 nm we noted a rapid degradation of these NDs into graphite. We attribute this to the large surface-to-volume ratio of small NDs and consequent absorption of the near-infrared pulsed excitation from sp^2 and/or organic surface groups causing relaxation of diamond

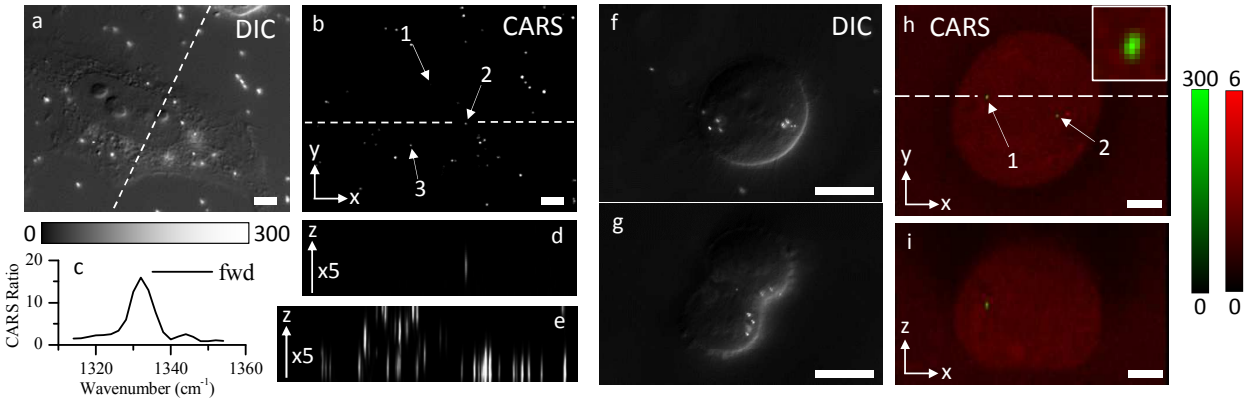

FIG. 5. **CARS imaging of single NDs in fixed and living cells.** DIC of a fixed HeLa cell (**a**) and corresponding fwd-CARS image (**b**) at the ND resonance of 1332/cm as maximum intensity projection over a 3 μm thick z-stack. Several NDs are observed, and three of them are specifically numbered (see text). **c**, fwd-CARS spectrum over a single ND in **b**. The CARS xz image along the x line cut over ND 2 in **b** is shown in **d**. **e**, CARS sections along the oblique line in **a** as maximum intensity projection perpendicular to it. The CARS ratio relative to the surrounding aqueous buffer is indicated in the gray-scale bar. Pump (Stokes) power on the sample was 22 mW (14 mW). 100 nm xy pixel size and 300 nm z step. 0.1 ms pixel dwell time. DIC of a live dividing HeLa cell just before (**f**) and after (**g**) the CARS images in **h**, **i**. xy fwd-CARS image at an axial depth in the center of the cell (different z-plane from **f**) (**h**), and corresponding xz image (**i**) along the x line cut shown in **h**. CARS measured at the ND resonance of 1332/cm (green) is overlayed with CARS measured at 2850/cm (red) showing the overall cellular structure at the CH stretch bond resonance. The inset is a 1.5 μm$\times$1.5 μm zoom over ND 1. The CARS ratio is indicated in the corresponding color bar. Pump (Stokes) power on the sample was 8 mW (6 mW). 100 nm xy pixel size and 500 nm z step. 0.01 ms pixel dwell time. All scale bars are 5 μm. Note the 5-fold zoom of the z-axis in **d** and **e**.

into the more energetically stable graphite structure. Noticeably, near-infrared two-photon excitation (similar to that in our CARS experiment) of NV centers in lipid-functionalised NDs of only $\sim$ 20 nm radii was recently reported [10], suggesting that careful engineering of the ND surface groups could overcome this absorption and consequent degradation. A detailed study of this effect is open to further research.

QUANTITATIVE CARS IMAGING OF NANODIAMONDS IN CELLS

As a proof-of-principle of the applicability of these non-fluorescing NDs for cell imaging, CARS microscopy of NDs internalized via endocytosis in HeLa cells after incubation overnight is shown in Fig. 5. A fixed HeLa cell imaged with DIC (at 10° polariser angle in the de Sénarmont compensator) is shown in Fig. 5a, and Fig. 5b gives the forward-detected CARS image at the 1332/cm ND resonance over the same area as maximum intensity projection from a z-stack of $3\,\mu$m thickness. The fwd-CARS ratio is quantified by dividing the measured CARS intensity with the fwd-collected CARS intensity in the aqueous buffer region outside the cell. NDs are clearly resolved, as we verified by performing spectral scans exhibiting the ND resonance (see Fig. 5c). Based on the calibration in Fig. 4e the strength of the fwd-CARS ratio can be used to quantify the ND size (assuming that they are single NDs). For the NDs indicated in Fig. 5b we find CARS ratios ranging from about 25 (ND 1) to nearly 300 (ND 3) well within the distribution in Fig. 4e and corresponding to radii from 105 nm to > 150 nm. Fig. 5d shows an axial cross-section along the x line-cut crossing through ND 2 (ratio of about 125). Fig. 5e gives an overview of the axial scans along the oblique line in Fig. 5a as maximum intensity projection perpendicular to it, from which we can see NDs following the cell axial profile above the glass coverslip surface. We also imaged NDs in living HeLa cells. HeLa cells undergoing division imaged with DIC just before and after the CARS acquisition are shown Fig. 5f,g. Cells continued to divide after acquisition, consistent with the observation by us and others [14] that CARS exciting beams in the near-infrared at time-averaged power densities in the MW/cm^2 range ($\sim 10\,$GW/cm^2 peak powers) comparable or lower than conventional two-photon fluorescence do not compromise cell viability. Fig. 5h shows a xy CARS image at an axial depth approximately in the center of the cell, and Fig. 5i shows the axial cross-section along the x line-cut indicated. Fwd-CARS at the 1332/cm ND resonance (green) is overlayed with fwd-CARS taken at 2850/cm in resonance with CH stretch bonds which provides an overall image of the cell. NDs are well visible inside the cell, as also confirmed by the axial cross-section. The strength of their fwd-CARS ratio at 1332/cm is about 190 (ND 2) and 300 (ND 1) indicating large NDs with radii of about 140 nm and above (the inset in Fig. 5h shows a zoom over ND 1 from which we deduce a CARS intensity FWHM of $0.3\,\mu$m in xy, bigger than the one in Fig. 3b).

We note that vibrationally non-resonant four-wave mixing has been reported on nanopar-

ticles of various materials, including gold [20, 21], metal-oxides [22], silicon [23] and carbon nanotubes [24], as also reviewed in Ref. [25]. However, strongly absorbing (e.g. metallic) nanoparticles create considerable photothermal heating upon electronic four-wave mixing excitation. Moreover vibrationally non-resonant four-wave mixing is not chemically specific and thus much less suited to selectively distinguish a nanoparticle type of interest. Notably, for diamond we measured that the vibrationally resonant susceptibility is $\sqrt{250}$ times higher than the non-resonant part and the Raman linewidth is very sharp (< 5/cm) which makes vibrationally resonant CARS a very sensitive and specific way to detect diamond nanoparticles.

CONCLUSIONS

In conclusion, we have shown that non-fluorescent single nanodiamonds have a strong CARS signal at the intrinsic sp^3 vibrational resonance of diamond which can be used for imaging. Importantly, we have quantified the relationship between the CARS signal strength and the ND size from which we inferred a size limit below 30 nm radius for a single ND imaged at excitation powers and acquisition speeds compatible with live cell imaging. This size range is of importance and practical use for drug delivery, cancer therapeutics [19] and contrasts agents *in vivo* [4]. The calibrated CARS signal strength in turn enables a quantitative analysis *in situ* of the size of NDs being internalized inside cells, as exemplified here by proof-of-principle images in fixed and living HeLa cells. Owing to the high biocompatibility of NDs, this opens the exciting prospect of unraveling complex trafficking pathways in living cells in a robust quantitative way, as opposed to fluorescence readouts.

METHODS

Nanodiamonds. Nanodiamond powders containing monocrystalline blocky particles in the 150-300 nm size range were purchased from L.M. Van Moppes and Sons SA (product code SYP 0.25-0.5). These powders are relatively inexpensive to fabricate by milling larger diamonds produced by high-pressure, high-temperature synthesis. Note that the ND powder appeared white, indicating negligible absorption from sp^2 surface carbon. NDs were purified in house via air annealing at 450-550°C which also resulted in the formation of surface

carboxyl groups. NDs were covalently attached onto gridded glass coverslips for single particle correlative studies (for more details see supplementary information, S1).

Electron microscopy TEM was performed on a JEM-2100 LaB6 Transmission Electron Microscope(Jeol Ltd.) utilising a high resolution digital camera (Gatan Inc.). SEM was performed using the inLens detector of a Raith e-Line system operating at 10 kV acceleration voltage and 10 mm working distance. Prior to SEM, a $\sim$ 40 nm gold layer was sputtered onto the ND covered coverslip to prevent charging.

Optical micro-spectroscopy. Confocal Raman spectra were taken using a Ti-U Nikon microscope stand with a 20x 0.75NA objective (bulk diamond sample) or a 60x 1.27NA water immersion objective (NDs). A 532 nm cw laser excitation was filtered with a Semrock laser line filter (LL01-532) and coupled into the microscope by a dichroic mirror (Semrock LPD01-532RS) with a power of 10 mW at the sample. Raman scattering was collected in epi-direction, filtered with a long pass filter (Semrock BLP01-532R), dispersed by an imaging spectrometer (Horiba iHR550) with a 150 lines/mm grating and detected with a CCD Camera (Andor Newton DU971N-BV) with a FWHM spectral resolution of about 10/cm. The absolute Raman cross-section of the 1332/cm line per atom in bulk diamond is reported to be about $4 \times 10^{-29}\,\mathrm{cm}^2$ with 515 nm excitation wavelength, decreasing with increasing wavelength to about $1 \times 10^{-29}\,\mathrm{cm}^2$ at 1064 nm [26]. The Raman signal scales linearly with the number of atoms in the focal volume. From this cross-section we can estimate the Raman signal in our experimental conditions. For a $(200\,\mathrm{nm})^3$ nanodiamond volume we find 7.6×10^5 photons/sec. Considering a collection solid angle of 20% of 4π and a detection efficiency of 10%, this results in about 1.5×10^4 photons/s detected with our confocal Raman setup. For the single ND shown in Fig. 1 we have integrated for 10 s and measured 1.1×10^5 detected photons in the 1332/cm peak (taking the number of counts and the nominal photoelectrons/count of the camera). Considering that the ND volume in Fig. 1 is not precisely known, this value is in good agreement with the estimate based on the Raman cross-section.

Scattering and extinction cross-sections were measured using the set-up and technique described in [16]. CARS was measured using the set-up and technique described in [17] with a 60x 1.27NA water immersion objective and a 1.4NA oil condenser. qDIC is performed using the set-up and technique described in [18] with a 60x 1.27NA water immersion objective and a 1.4NA oil condenser. For more details, see also supplementary information. For the

correct quantification of the CARS intensity ratio, backgrounds were measured under the same excitation and detection conditions with Pump and Stokes pulses out of time overlap, and were then subtracted from the measured CARS intensities.

Hela cells. HeLa (A.T.C.C. CCL-2) cells were grown on 25 mm-diameter coverslips in DMEM (Dulbeccos modified Eagles medium; Life Technologies) medium supplemented with 10% (v/v) FCS (foetal calf serum) and 2 mM L-glutamine. Cells were incubated over night with a solution containing NDs in RPMI medium (Life Technologies) supplemented with 10% (v/v) FCS and 2 mM L-glutamine. For fixed cell studies HeLa cells were fixed with 4% paraformaldehyde in PBS and mounted onto a glass slide using a 120 μm thick imaging gasket filled with water. For live cell studies, coverslips with live HeLa cells were mounted onto a glass slide using a 120 μm thick imaging gasket filled with 15 μL of RPMI medium containing FCS and 25 mM HEPES as a pH stabilising buffer. Samples were placed in the microscope environmental chamber and maintained at 37°C for live cell CARS imaging.

---

* borrip@cardiff.ac.uk

[1] Schrand, A. M., Ciftan Hens, S. A. & Shenderova, O. A. Nanodiamond particles: Properties and perspectives for bioapplications. *Crit. Rev. Solid State Mater. Sci.* **34**, 18–74 (2009).

[2] Mochalin, V. N., Shenderova, O., Ho, D. & Gogotsi, Y. The properties and applications of nanodiamonds. *Nat. Nanotechnol.* **7**, 11–23 (2012).

[3] Kaur, R. & Badea, I. Nanodiamonds as novel nanomaterials for biomedical applications: drug delivery and imaging systems. *Int. J. Nanomed.* **8**, 203–220 (2013).

[4] Wu, T.-J. *et al.* Tracking the engraftment and regenerative capabilities of transplanted lung stem cells using fluorescent nanodiamonds. *Nat. Nanotechnol.* **8**, 682–689 (2013).

[5] Weng, M.-F., Chang, B.-J., Chiang, S.-Y., Wang, N.-S. & Niu, H. Cellular uptake and phototoxicity of surface-modified fluorescent nanodiamonds. *Diamond Relat. Mater.* **22**, 96–104 (2012).

[6] Liu, K.-K., Wang, C.-C., Cheng, C.-L. & Chao, J.-I. Endocytic carboxylated nanodiamond for the labeling and tracking of cell division and differentiation in cancer and stem cells. *Biomaterials* **30**, 4249–4259 (2009).

[7] Krueger, A. & Lang, D. Functionality is key: Recent progress in the surface modification of

nanodiamond. *Adv. Funct. Mater.* **22**, 890–906 (2012).

[8] Neugart, F. *et al.* Dynamics of diamond nanoparticles in solution and cells. *Nano Lett.* **7**, 3588–3591 (2007).

[9] McGuinness, L. P. *et al.* Quantum measurement and orientation tracking of fluorescent nanodiamonds inside living cells. *Nat. Nanotechnol.* **6**, 358–363 (2011).

[10] Hui, Y. Y. *et al.* Two-photon fluorescence correlation spectroscopy of lipid-encapsulated fluorescent nanodiamonds in living cells. *Opt. Express* **18**, 5896–5905 (2010).

[11] Grotz, B. *et al.* Charge state manipulation of qubits in diamond. *Nat. Comm.* **3:729** (2012).

[12] Smitha, B. R., Niebertc, M., Plakhotnika, T. & Zvyagin, A. V. Transfection and imaging of diamond nanocrystals as scattering optical labels. *J. Lumin.* **127**, 260–263 (2007).

[13] Perevedentseva, E. *et al.* The interaction of the protein lysozyme with bacteria e. coli observed using nanodiamond labelling. *Nanotechnology* **18**, 315102 (2007).

[14] Zumbusch, A., Langbein, W. & Borri, P. Nonlinear vibrational microscopy applied to lipid biology. *Prog. Lipid Res.* **52**, 615–632 (2013).

[15] Osswald, S., Mochalin, V. N., Havel, M., Yushin, G. & Gogotsi, Y. Phonon confinement effects in the Raman spectrum of nanodiamond. *Phys. Rev. B* **80**, 075419 (2009).

[16] Payne, L. M., Langbein, W. & Borri, P. Polarization-resolved extinction and scattering cross-section of individual gold nanoparticles measured by wide-field microscopy on a large ensemble. *Appl. Phys. Lett.* **102**, 131107–1 (2013).

[17] Pope, I., Langbein, W., Watson, P. & Borri, P. Simultaneous hyperspectral differential-CARS, TPF and SHG microscopy with a single 5 fs Ti:Sa laser. *Opt. Express* **21**, 7096–7106 (2013).

[18] McPhee, C. I., Zoriniants, G., Langbein, W. & Borri, P. Measuring the lamellarity of giant lipid vesicles with differential interference contrast microscopy. *Biophys. J.* **105**, 1414–1420 (2013).

[19] Davis, M. E., Chen, Z. & Shin, D. M. Nanoparticle therapeutics: an emerging treatment modality for cancer. *Nat. Rev. Drug Discovery* **7**, 771–782 (2008).

[20] Kim, H., Taggart, D. K., Xiang, C., Penner, R. M. & Potma, E. O. Spatial control of coherent anti-stokes emission with height-modulated gold zigzag nanowires. *Nano Lett.* **8**, 2373–2377 (2008).

[21] Masia, F., Langbein, W., Watson, P. & Borri, P. Resonant four-wave mixing of gold nanoparticles for three-dimensional cell microscopy. *Opt. Lett.* **34**, 1816–1818 (2009).

[22] Moger, J., Johnston, B. D. & Tyler, C. R. Imaging metal oxide nanoparticles in biological structures with CARS microscopy. *Opt. Express* **16**, 3408–3419 (2008).

[23] Jung, Y., Tong, L., Tanaudommongkon, A., Cheng, J. X. & Yang, C. In vitro and in vivo nonlinear optical imaging of silicon nanowires. *Nano Lett.* **9**, 2440–2444 (2009).

[24] Kim, H., Sheps, T., Collins, P. G. & Potma, E. O. Nonlinear optical imaging of individual carbon nanotubes with four-wave-mixing microscopy. *Nano Lett.* **9**, 2991–2995 (2009).

[25] Wang, Y., Lin, C.-Y., Nikolaenko, A., Raghunathan, V. & Potma, E. O. Four-wave mixing microscopy of nanostructures. *Adv. Opt. and Photonics* **3**, 1–52 (2011).

[26] Aggarwal, R., Farrar, L., Saikin, S., Andradeb, X. & amd D.L. Polla, A.-G. Measurement of the absolute Raman cross section of the optical phonons in type Ia natural diamond. *Solid State Commun.* **152**, 204–209 (2012).

ACKNOWLEDGMENTS

The authors acknowledge the Cardiff University Large Research Equipment Fund for providing high-resolution TEM facilities, and thank Dr. Georgi Lalev and Kez Cleal for their assistance. This work was funded by the UK BBSRC Research Council (grant n. BB/J021008/1 and BB/H006575/1). PB acknowledges the UK EPSRC Research Council for her Leadership fellowship award (grant n. EP/I005072/1).

AUTHOR CONTRIBUTIONS

P. B. and W. L. conceived and designed the experiments, interpreted the results and wrote the manuscript. I. P. performed the CARS experiments and analysed the data. L.P. performed the optical extinction cross-section measurements and analysed the data. G. Z. performed the quantitative DIC experiments and analysed the data. E. T. performed the SEM experiments and analysed the data. O.W. provided the bulk diamond and ND materials. P.W. performed the cell culture work. All authors discussed the results and commented on the manuscript.